FULL PAPER

Insights into plasma-assisted polymerization at atmospheric pressure by spectroscopic diagnostics

Federica Barletta[1] | Christophe Leys[2] | Vittorio Colombo[1,3] | Matteo Gherardi[1,3] | Nikolay Britun[4] | Rony Snyders[4] | Anton Nikiforov[2]

[1]Department of Industrial Engineering (DIN), Alma Mater Studiorum Università di Bologna, Bologna, Italy

[2]Department of Applied Physics, Ghent University, Ghent, Belgium

[3]Industrial Research Center for Advanced Mechanics and Materials (C.I.R.I.-M.A.M.), Alma Mater Studiorum Università di Bologna, Bologna, Italy

[4]Chimie des Interactions Plasma-Surface (ChIPS), CIRMAP, Université de Mons, Mons, Belgium

Correspondence

Federica Barletta, Department of Industrial Engineering (DIN), Alma Mater Studiorum Università di Bologna, Via Terracini 24, 40131 Bologna, Italy. Email: federica.barletta3@unibo.it

Abstract

In the present work, a polydiagnostic study of an atmospheric pressure plasma jet specifically designed for the deposition of coatings by using an Ar/tetraethyl orthosilicate (TEOS) mixture is undertaken. Both passive and active diagnostic methods are utilized to shed light on the complexity of gas-phase mechanisms of precursor fragmentation. A detailed characterization is performed by (fast imaging) optical emission spectroscopy (OES) to clarify the spatial–temporal behavior of excited species. The influence of the TEOS admixture on gas temperature is studied by OES and Rayleigh scattering techniques. The evolution of streamers and their influence on radical formation in the treatment zone is also discussed.
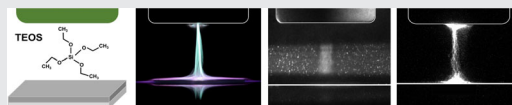
KEYWORDS

active species, laser scattering, plasma diagnostics, plasma jet, plasma polymerization

1 | INTRODUCTION

Various applications of atmospheric pressure plasmas for deposition of Si-based thin films on thermosensitive polymers have high industrial potential in a variety of fields, including food/beverage packaging and biomedical devices, due to economic and technological advantages in comparison with state-of-the-art vacuum coating techniques.[1,2] Until now, different atmospheric plasma configurations have been described in the literature for the deposition of Si-based coatings, and a number of process parameters, which have a significant effect on the properties of the plasma-synthesized film, have been highlighted.[3–6] In this respect, the suitability to perform local treatments of complex 3D surfaces and the possibility of varying the treatment zone scale from a few square centimeters down to the submillimeter range makes the atmospheric pressure plasma jet (APPJ) one of the most promising plasma sources for Si-based thin

film deposition. The use of different jet geometries, the effect of an air/oxygen admixture, and the impact of different pulse repetition frequencies and substrate temperature on thin-film features have already been investigated in the past.[7,8] However, despite the good understanding of APPJ-related processes[9–11] as well as the successful results obtained by several research groups in terms of thin-film properties with APPJs,[12,13] further optimization of the deposition process based on the obtained results requires a higher level of understanding of both the discharge physics and the chemical gas-phase mechanisms involved.

Attainment of a clear correlation between the chosen plasma parameters and the chemical and morphological features of the plasma-deposited films is of particular interest for the APPJs working in Ar/tetraethyl orthosilicate (TEOS) mixtures.[14] In fact, among the variety of possible organosilicon monomers, the choice of TEOS as a precursor has recently gained wide interest in the case

of atmospheric pressure plasmas as it is easily convertible into Si-based thin films possessing low organic content and thus suitable for a large number of applications such as improvement of packaging barrier properties.[15] However, the lack of clarity related to the dominant gas-phase reactions and the complete absence of reference data about monomer fragmentation pathways in the case of Ar/TEOS plasma atmospheric deposition is actually one of the main barriers to an adequate control over the process and coatings properties.

As a first step toward a detailed study of the most significant gas-phase processes having a key role in the thin film features definition, the use of integrated time- and space-resolved discharge diagnostics is strongly anticipated. Diagnostics-wise, most research has been performed with the use of optical emission spectroscopy (OES) until now, mainly due to its nonintrusiveness and easy-to-setup features as well as due to the fact that OES provides information about the excited plasma species.[16,17] Even if the density of emitters in plasma is much lower than the density of species in the ground state, the use of emission-based techniques is an important first step for an in-depth understanding of any plasma process.[18,19]

The OES technique is combined in this study with the polydiagnostics of an APPJ for the deposition of Si-based thin films by using an Ar/TEOS mixture. Even though the use of the abovementioned APPJ has already been considered by some authors for the polymerization of biocompatible amine/amide-rich coatings, the use of such a plasma source for Si-based thin films polymerization remains so far unexplored.[20] Thus, addressing the abovementioned issues, the aim of this study is twofold: (a) to study the TEOS influence on the plasma gas

temperature, electron density, and spatial–temporal behavior of excited species in an Ar/TEOS APPJ; (b) to shed light on the predominant gas-phase mechanisms in the presence of heavy molecules of TEOS leading to deposition of organosilicon coatings. High-resolution spectra of the OH(A-X), N_2(C-B), and CH(A-X) emission bands have been used for rotational temperature measurements and the conditions for which these temperatures can be assumed equal to the gas temperature (T_{gas}) in the case of the Ar/TEOS mixture are discussed. The applicability of the Rayleigh scattering method for T_{gas} measurements during a deposition process is further analyzed, and the time- and space-resolved behavior of the excited species have been used to discuss possible mechanisms involved in the excited state generation. Finally, some representative thin film surface characterization results, obtained by attenuated total reflectance-Fourier-transform infrared (ATR-FTIR) spectroscopy and scanning electron microscopy (SEM) analysis, are reported.

2 | EXPERIMENTAL SECTION

2.1 | Plasma deposition systemcalled

A schematic view of the setup used in this study is shown in Figure 1. The plasma source consists of a single electrode corona jet (called "AlmaJET" - see Figure 2 for details) well suited for localized plasma treatment and deposition of complex 3D coatings.[20,21] Ar gas flow of 2 standard liter per minute (slm) was injected in the discharge region through the primary channel; while, simultaneously, a second flow of 3 slm of Ar was introduced through the secondary gas channel in the
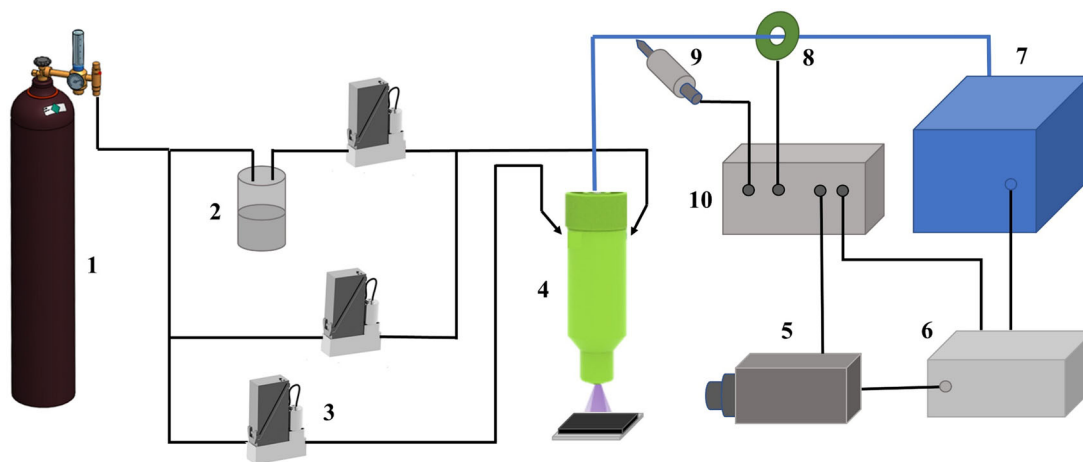
FIGURE 1 Layout of the plasma deposition setup: (1) Ar supply, (2) bubbling system, (3) digital mass flow controller, (4) plasma source, (5) intensified charge-coupled device camera, (6) synchronization unit, (7) high-voltage generator, (8) current probe, (9) voltage probe, (10) oscilloscope

FIGURE 2 Plasma discharge in (a) Ar or (b) Ar/TEOS mixture (no optical filtering); (c) the scheme of the APPJ source, APPJ, atmospheric pressure plasma jet; HV, high voltage; TEOS, tetraethyl orthosilicate
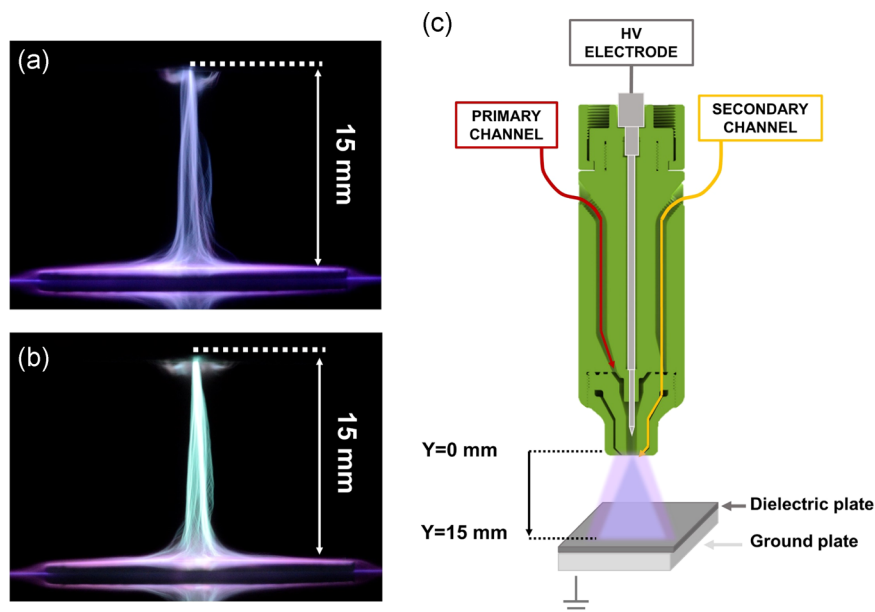
region downstream of the high-voltage (HV) electrode tip. The amount of precursor content, introduced in the primary channel of the system, was controlled by setting the flow of carrier gas (0.065 slm of Ar) passing through a bubbling system filled with TEOS precursor ($SiO_4C_8H_{20}$, ≥99%; Sigma-Aldrich). The concentration of TEOS injected in the feed mixture, equal to 17 ppm, was calculated by assuming 20°C of gas-flow temperature and 1 Torr saturation pressure of TEOS.[22] The flow rates were controlled by digital mass flow controllers (EL-FLOW; Bronkhorst). The distance between the HV tip of the APPJ and the dielectric plate, which covers the ground electrode, was kept constant at 15 mm. The upper electrode was connected to an alternating current (AC) power supply (AlmaPulse, AlmaPlasma s.r.l.) operating at a frequency of 12 kHz and 12 kV of amplitude.

To measure the power applied to the plasma device, voltage and current waveforms were recorded by means of a Tektronix P6015A high-voltage probe and a Pearson 6585 current transformer connected to a Tektronix DPO40034 digital oscilloscope. The input power,

obtained based on these waveforms (see Figure 3) has been kept constant in all experiments at 11.5 W. The filamentary Ar and Ar/TEOS plasma discharges, shown in Figure 2a and 2b, respectively, are sustained in ambient air, so the air back diffusion has to be taken into account when discussing the obtained results.

2.2 | OES and fast imaging setup

The OES measurements were performed along the discharge axis at 7.5 mm from the APPJ head ($y = 0$) using an Andor Shamrock-750 spectrometer equipped with a 1,800 or 3,600 gr/mm diffraction grating and an Andor iStar 740 intensified charge-coupled device (ICCD) camera used as a detector. The plasma emission was guided to the spectrometer by using a UV-VIS optical fiber. The wide range spectra were measured with a resolution of 0.05 nm at FWHM (full width at half maximum), while the time-resolved spectra were recorded with a resolution of 0.03 nm, except for the case of H_α lines used for electron density calculation (0.048 nm).
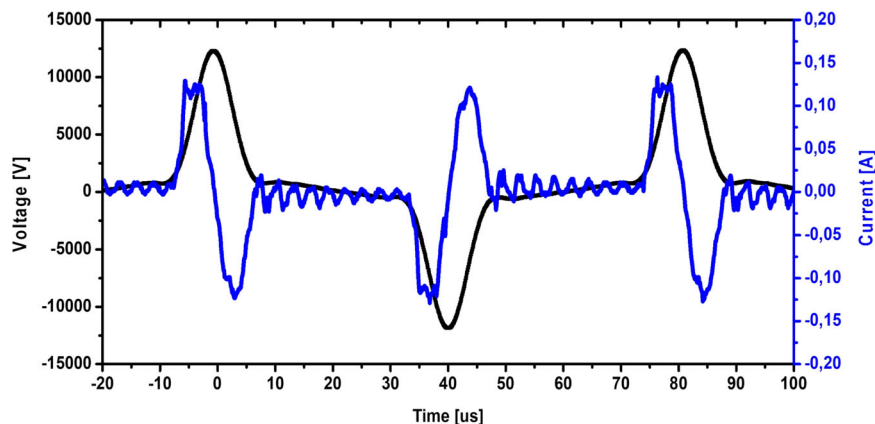
FIGURE 3 Voltage and current waveforms of the atmospheric pressure plasma jet used in this study acquired during the deposition process

In all the cases, time-resolved OES spectra have been acquired with a time-step of 1 μs.

The ICCD camera, equipped with a Cerco 100 mm f/2.8 UV lens transparent in the 220–900 nm range, was also used to capture time-resolved 2D OES images by applying five different bandpass filters with the central wavelength at 696, 780, 340, 309, and 430 nm to detect Ar, O, N_2, OH, and CH emission lines/bands, respectively. Single shot CH and OH images have been obtained with a gate time of 1 μs while 5 μs was used in the O atom case (due to low intensity). Radiation patterns of Ar I and N_2* were acquired at 2 μs of gate time. The ICCD camera was synchronized with the AC generator by means of a Stanford Research DG645 Digital Delay Generator and a TTL signal generator (synchronization unit in Figure 1). The time delay (starting from the positive voltage peak) was set at 2, 22, and 42 μs to reflect the discharge appearance during the positive and negative voltage half cycles as well as between the peaks.

2.3 | Gas temperature and electron density measurements

One of the most widespread methods for gas temperature (T_{gas}) measurements is the calculation of rotational temperature (T_{rot}) of excited diatomic molecules assuming that $T_{gas} \approx T_{rot}$. In the atmospheric pressure plasmas, however, the population of rotational states is often characterized by a prominent non-Boltzmann shape. Thus, in these cases, T_{rot} only reflects formation of specific excited states, not giving a reliable solution for gas temperature.[23,24] In this respect, various simulation softwares, such as Lifbase, are based on the assumption that rotational states are Boltzmann-distributed, and, as a consequence, a careful results analysis is strongly required. In the current work, rotational temperatures at the excited OH(A), N_2(C), and CH(A) states are determined by using two different software. For rotational temperature of the OH(A) state, it is known that only rotational states with small rotational numbers are capable of giving the real gas temperature.[25] For this reason, T_{rot} of OH radicals was obtained using MassiveOES software, which takes into account only rotational states with $J < 9$. These measurements were performed with and without precursor to verify how its presence affects T_{gas}. In contrast, T_{rot} of N_2 and CH excited molecules were determined by the fitting method using Lifbase software in a single T_{rot} approximation.

Numerous research groups have estimated T_{gas} from the rotational temperature of OH and N_2 excited states for different high-pressure plasmas so far. Bruggeman[26]

has shown that in the case of DC-excited discharges generated in water, OH cannot be used as a reliable estimate of T_{gas}, as high H_2O density leads to a significant overestimation with respect to the values obtained with the N_2(C-B) band. In addition, a similar study performed by Nikiforov[25] using an APPJ generated in Ar/water mixtures has proven that the T_{rot} of N_2 molecules is much higher than the expected temperature while T_{gas} is equivalent to the temperature determined by the first slope of the Boltzmann plot of OH radicals. In this study, the same issue has also been checked in the case of Ar/TEOS mixture to identify which of the two chosen molecules provide the best estimation for T_{gas}.

Considering TEOS fragmentation, accompanied by CH radical formation, T_{gas} measurements via high-resolution CH emission spectra are discussed in this paper for the first time. Although CH radicals are common byproduct of atmospheric pressure deposition of organosilicon precursors and CH band emission intensity is commonly used for estimation of the conversion rate toward Si-based thin films, the appearance of a distorted rotational distribution is very likely as a result of the complex CH formation process in Ar plasmas.[5] The appropriate analysis of CH emission may provide a convenient way to control deposition processes through the T_{rot} (CH) estimation and clarify the excitation mechanisms in the presence of TEOS in general.

It is known that precursor fragmentation strongly depends on plasma properties, such as the ionization degree. For electron density measurements under atmospheric pressure, Stark broadening of the hydrogen or hydrogen-like atomic spectral lines is the most widely used method.[26,27] In this study, a time-resolved H_α has been used to obtain the electron density evolution during the positive and negative voltage peaks for the case of Ar/TEOS APPJ. As is known, in the case of atmospheric discharges, the experimentally measured H_α line broadening represents convolution of different broadening mechanisms (corresponding to either Gaussian or Lorentzian line shapes). The Stark broadening estimation formula, in this case, is well known.[28,29] It is important, however, to highlight that in the case of APPJs, the natural- and resonance-broadening contributions are almost negligible, as reported by Nikiforov et al.[27] Doppler broadening, however, has been estimated in our case to be rather low as well (about 1.3 pm), which cannot considerably affect electron density calculation. Consequently, all broadening mechanisms with a Gaussian profile were neglected in this study, and only a convolution of several Lorentzian profiles was taken into account:

$$\Delta\lambda_{exp}(nm) \cong \Delta\lambda_s + \Delta\lambda_{VdW} + \Delta\lambda_{ins}, \qquad (1)$$

where $\Delta\lambda_s$, $\Delta\lambda_{VdW}$, and $\Delta\lambda_{ins}$ are the FWHM of Stark, Van der Waals, and instrumental broadening, respectively. $\Delta\lambda_{ins} = 0.048$ nm in our case (measured by an Hg line in a low-temperature plasma source). For $\Delta\lambda_{VdW}$ calculation, the formula suggested by Hofmann et al. was used.[30] Finally, electron density values were calculated as a function of $\Delta\lambda_s$ using the data tabulated by Gigosos et al.[31] in the case of the H_α line.

2.4 | Rayleigh scattering experiment

The experimental setup used in this study for Rayleigh scattering measurements is shown in Figure 4. As described in the previous studies,[32,33] this active spectroscopic technique is typically used for gas temperature measurement, as the scattering signal (I) is proportional to the density of heavy particles (n^i), which is, in turn, inversely proportional to the T_{gas} value at a constant pressure (p), as defined by the ideal gas law:

$$I \sim \sum_i \sigma^i n^i = \sum_i \sigma^i \frac{p}{T_{gas}k_B}, \qquad (2)$$

where k_B is the Boltzmann constant and σ^i is the Rayleigh scattering cross-section of heavy species at 532 nm.[34] Although in our case, the APPJ works in ambient air, the Rayleigh scattering signal can be considered independent of the percentage of air in the gas mixture as the scattering cross-sections of Ar $(5.4 \times 10^{-32} \, m^2)$, N_2 $(6.2 \times 10^{-32} \, m^2)$, and O_2 $(5.3 \times 10^{-32} \, m^2)$ are all comparable.[35] Next, by using the relation $T_{gas}I = T_{ref}I_{ref}$, it is possible to deduce T_{gas} in the plasma area from the Rayleigh scattering signal (I) and a reference measurement (I_{ref}) obtained with the Ar gas flow on and the plasma discharge off at a known ambient gas temperature ($T_{ref} = T_{amb}$). Correspondingly, the laser scattering method is well suited for validation of the emission spectroscopy results, namely the T_{rot} values obtained using OH, CH, and N_2 excited states.

In our experiments, the laser scattering measurements were done by using a pulsed Nd:YAG laser (Litron Nano S), operating at 532 nm with a pulse energy of 8 mJ, a repetition rate of 10 Hz, and 8 ns of pulse duration. The scattered light was collected perpendicularly to the laser beam by a fast imaging gated Hamamatsu digital camera with a 532 nm filter ($\Delta\lambda_{FWHM} = 10$ nm) and 500 ns of exposure time to obtain a superior image quality and compensate jitter. The setup used to synchronize the ICCD camera with the laser is similar to the one used for time-resolved OES measurement. For all T_{gas} measurements, the laser beam, characterized by a size of 8×0.1 mm, was passing through the plasma discharge at a distance of 7.5 mm from the gas outlet to avoid beam reflection from either the dielectric plate or the APPJ head. The Rayleigh scattering method has higher sensitivity compared to the rotational analysis resulting in a T_{gas} accuracy of ± 15 K.

2.5 | Thin-film surface characterization

Si-based thin films were deposited onto polypropylene (PP) foils of 0.5 mm thickness and 25 mm width (Goodfellow, UK). The thin film chemical structure was analyzed by ATR-FTIR spectroscopy, where the spectra were acquired by using an Agilent Cary 660 spectrometer with 32 scans at a spectral resolution of 2 cm^{-1}. Thin film morphology was investigated by means of a Phenom G2 ProX scanning electron microscope by applying an accelerating voltage of 10 kV. A sputter coater (SC7620;
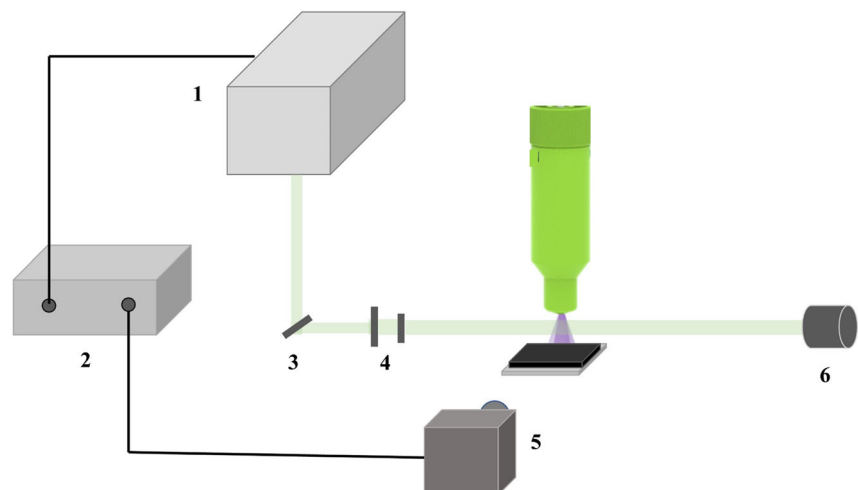
FIGURE 4 Rayleigh scattering spectroscopy setup including (1) Nd:YAG laser at 532 nm, (2) synchronization unit, (3) prism, (4) sheet forming optics, (5) intensified charge-coupled device camera, (6) beam dump

Quorum Technologies) was used to cover the thin film surface with gold-palladium before SEM analysis.

3 | RESULTS AND DISCUSSION

3.1 | Emission spectra analysis and T_{gas} measurements

TEOS injection in the discharge region does not perturb the emission spectrum drastically (compared with the pure Ar discharge case), as shown in Figure 5. For the sake of clarity, the low-resolution spectrum here is divided into two wide spectral ranges (300–670 and 690–850 nm), by using an exposure time of 200 and 5 ms respectively. Most of the emission lines located between 690 and 850 nm (Figure 5b), corresponding to the Ar $4p \rightarrow 4s$ transitions, are characteristic of atmospheric pressure Ar plasma; while a significant emission from the nitrogen second positive system ($N_2(C\text{-}B)$) and the hydroxyl radicals' (OH ($A\text{-}X$)) band is observed between 300 and 650 nm (Figure 5a), due to the presence of the surrounding air and water vapor traces.[36] Moreover, the addition of TEOS leads to the appearance of the CH, CN, and

C_2 emission bands, as a result of its fragmentation by electron impact or Ar metastable collisional processes.[37] The detailed line and rotational band assignments for the mentioned atoms and molecules are given in Table 1.

It is important to bear in mind that the APPJ described in this study has been specifically applied for the deposition of thin films on thermosensitive materials. As a consequence, among various physical plasma properties, gas temperature is one of the key parameters for adequate control of the deposition process. Apart from having a strong influence on the kinetics of gas-phase reactions and in-flight particle nucleation, T_{gas} has a central role in the definition of thin-film properties. As demonstrated in several studies, in the case of deposition on a polymeric substrate, high processing temperature may result in severe morphological defects, such as crack formation, thereby hampering industrial applicability of the films.[38] Thus, this key parameter should be carefully controlled to maintain an appropriate temperature of the heat-sensitive surfaces.

To address this point, two different spectroscopic methods for T_{gas} measurement have been applied. As a
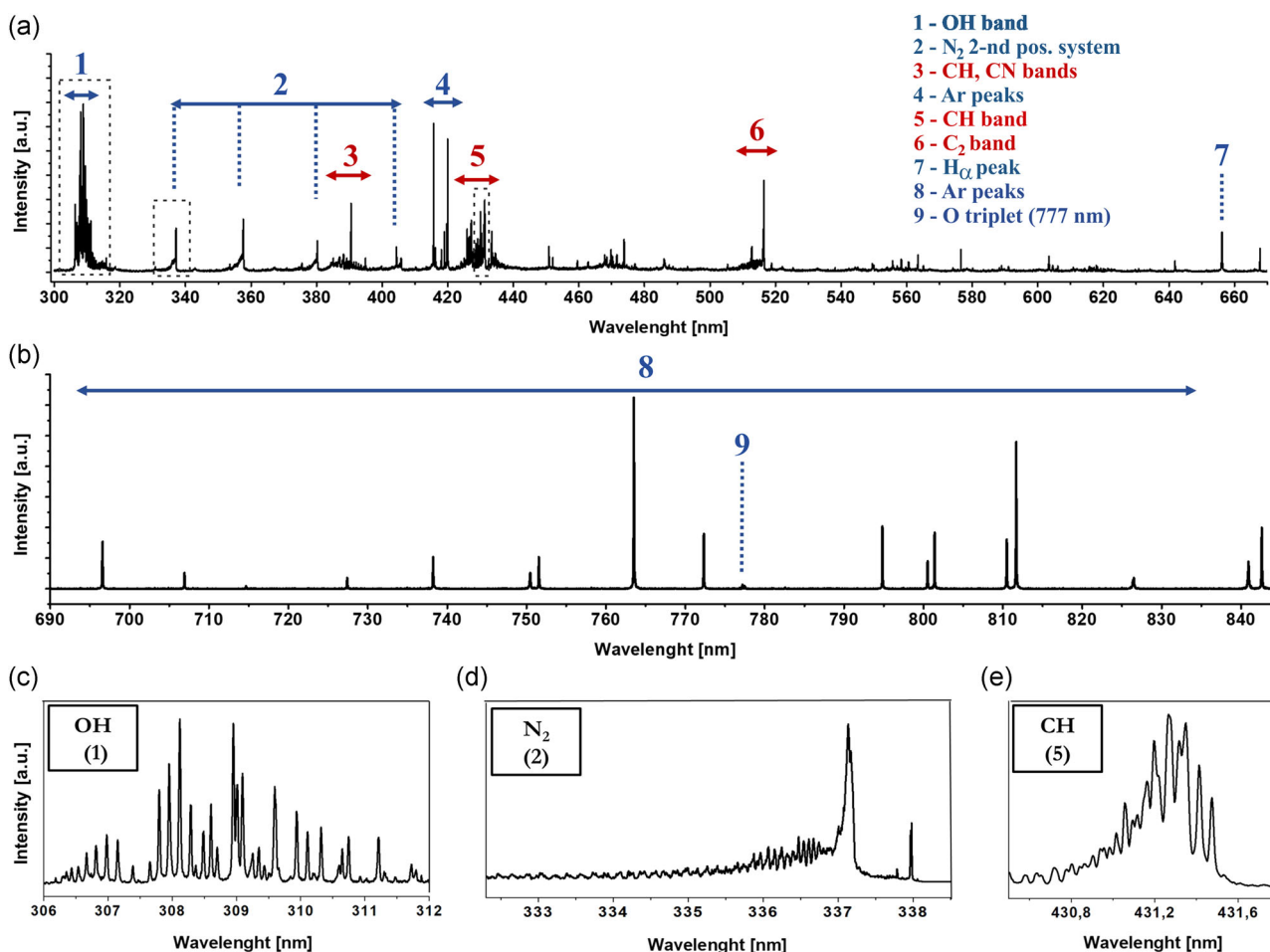
FIGURE 5 Overview and high-resolution spectra in Ar/TEOS mixture: (a) 300–650 nm, (b) 690–840 nm, (c) 306–312 nm → OH($A\text{-}X$), (d) 332–338 nm → $N_2(C\text{-}B)$, (e) 430–432 nm → CH($A\text{-}X$) measured at the negative voltage peak at 42 μs time delay. Molecular bands marked by red numbers appear as a result of TEOS addition. TEOS, tetraethyl orthosilicate

TABLE 1 Detailed spectra assignment in Ar/TEOS mixture

No.	Species	Transition	λ (nm)
1	OH	$A^2\Sigma^+ \rightarrow X^2\Pi$	308.9
2	N_2	$C^3\Pi_u \rightarrow B^3\Pi_g$	337.1
3	CH	$B^2\Delta \rightarrow X^2\Pi$	388.9
	CN	$B^2\Sigma \rightarrow X^2\Sigma$	386.2, 387.1
4	Ar I	$3p_5 \rightarrow 1s_4$	419.83
		$3p_9 \rightarrow 1s_5$	420.06
5	CH	$A^2\Delta \rightarrow X^2\Pi$	431.3
6	C_2	$d^3\Pi_g \rightarrow a^3\Pi_u$	518.0
7	H_α	$2p \rightarrow 3d$	656.28
8	Ar I	$2p_2 \rightarrow 1s_5$	696.54
		$2p_1 \rightarrow 1s_2$	751.46
		$2p_6 \rightarrow 1s_5$	763.51
		$2p_2 \rightarrow 1s_3$	772.42
		$2p_4 \rightarrow 1s_3$	794.81
		$2p_9 \rightarrow 1s_5$	826.45
9	O I	$3p \rightarrow 3s$	777.41

Abbreviation: TEOS, tetraethyl orthosilicate.

TABLE 2 OH, N_2, and CH rotational temperature mean values calculated in Ar or Ar/TEOS mixture by using 0.03 nm of spectral resolution

Primary gas flow	Excited species	Rotational temperature (K)
Ar	OH (A-X)	382 ± 50
Ar	N_2 (C-B)	549 ± 50
Ar/TEOS	OH (A-X)	409.7 ± 50
Ar/TEOS	N_2 (C-B)	551.6 ± 50
Ar/TEOS	CH (A-X)	590 ± 50

Abbreviation: TEOS, tetraethyl orthosilicate.

first step, OES has been used for rotational temperature calculation of the OH $A^2\Sigma^+ \rightarrow X^2 \Pi_i$ (0,0), N_2 C $^3\Pi_u \rightarrow$ B $^3\Pi_g$ (0,2), and CH $A^2\Delta \rightarrow X^2\Pi$ (0,0) molecular emission bands. The OH, N_2, CH high-resolution spectra acquired at the negative voltage peak (42 µs) in the Ar/TEOS mixture are reported in Figure 5, and the results of the measurements are summarized in Table 2. As expected, taking into account the low percentage of TEOS introduced as well as the measurement accuracy, the precursor injection has a nonsignificant impact on T_{rot} of the abovementioned N_2 and OH molecules. However, from Table 2, it is clear that T_{rot} obtained using N_2 and CH bands (~550–590 K) are considerably higher than the value estimated from OH transition (~410 K).

These experimental results corroborate with several previous studies claiming overestimation of T_{gas} obtained by N_2 emission bands in the case of Ar plasma generated in ambient air, due to the presence of Ar metastables (Ar^m) leading to production of $N_2(C)$ excited molecules by a quasi-resonance process (see Equation (6) in Section 3.3).[25]

Surprisingly, the T_{rot} results obtained with CH band are very similar to those obtained with N_2, contradicting at the same time, the OH-based T_{rot} values. As the use of CH emission for T_{gas} estimation has never been discussed for atmospheric pressure deposition processes with TEOS as precursor, further efforts are required to understand the observed disagreement. It is well known that the rotational distribution of excited diatomic molecules formed by direct electron impact from the respective ground state normally corresponds to rotational distribution in the ground state.[24] Nevertheless, the presence of TEOS-related dissociation reactions, electron impact dissociative excitation, and Penning reactions have to be taken into account to understand the pathways of CH radical formation.

The simplified model for CH radical formation in our case is given in Figure 6. As reported by Okimura et al.,[39] at the electron energy below 8–9 eV the first products of TEOS dissociation are most likely hydrocarbon fragments such as C_2H_4 and C_2H_5, while at the energy around 15 eV (which exceeds the energy of Ar $1s_5$ state), CH_3 and $Si_x(C_2H_5O)_y$ stable fragments are mainly formed. Moreover, during the deposition process, several ionized fragments, produced by dissociative ionization of TEOS molecules, can further affect CH(A) radical production. For example, as shown by Kawaguchi et al.,[40] the highest partial ionization cross-sections corresponding to $SiO_4C_6H_{15}^+$ (8×10^{-16} cm²) and $OC_2H_5^+$ (3×10^{-17} cm²) ionized fragment pathways require about
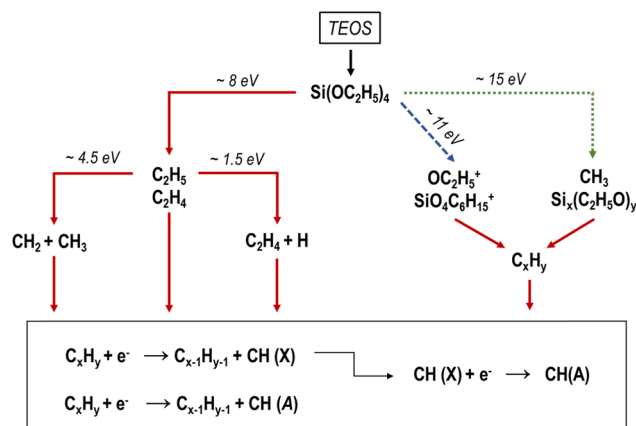
FIGURE 6 Main formation pathways of CH(A) radicals; — electron impact dissociative reactions, - - - Ar metastable collisions, · · · · dissociative reactions

11–12 eV of electron energy, which is close to the Ar^m energy level. Moreover, despite the absence of detailed information about the products and rate coefficients in the case of Ar^m–TEOS reactions, Le Brizoual[41] has shown that TEOS molecules quench Ar metastable atoms nearly as fast as oxygen. Therefore, by assuming the same quenching rate constant reported by Piper[42] for Ar^m–O_2 collisions (2.1×10^{-10} cm^2/s), it is possible to hypothesize a dominant role of Ar^m in the TEOS dissociation processes due to very fast reaction kinetics.

Nevertheless, in general, it can be stated that the primary products of TEOS fragmentation induced by electron impact and collisions with Ar^m are the C_2 hydrocarbons and the Si-containing fragments. These species can be further dissociated contributing to $CH(A)$ radical production. Several authors have shown that C_2H_5 and C_2H_4 fragments can be in turn defragmented into CH, CH_2, and CH_3 radicals. For instance, the work of Steinbauer et al.[43] reported that about 4.67 eV is required for dissociation of C_2H_5 to $CH_3(^2A_2'')$ and $CH_2(^3B_1/^1a_1)$, while only 1.57 eV is required for dissociation of C_2H_5 leading to $C_2H_4(X^1A_g)$ and H atoms.[43] The latter mechanism is a very probable dominant pathway in the case of the Ar-based plasma jet with a mean electron energy of about 1 eV.[25] As a consequence, CH_3–CH radicals are likely the main products of TEOS fragmentation and the primary source of $CH(A)$ radical production, visible in our OES spectra (see Figure 5).

In general, the $CH(A)$ excited state can be populated by electron impact dissociative excitation of hydrocarbons, such as CH_3–CH, by high energy electrons (around 14 eV) or by direct excitation of the previously dissociated ground state CH by low energy electrons.[44]

In spite of the suggestions given above, the exact mechanisms of CH_3–CH radical defragmentation into CH (A) and $CH(X)$ radicals in the case of Ar/TEOS plasmas remain hidden. Assuming the C–C bond dissociation energy of about 3.6–3.9 eV and a required excitation energy of ~4–6 eV for $CH(X)$ to $CH(A)$ excitation, there are number of possible mechanisms through reactions with OH radicals, Ar^m and other excited particles, which could influence rotational distribution of the $CH(A)$ state.[45] Moreover, this distribution might also be nonthermal, resulting in considerably higher values of T_{rot} compared with those observed in our case. Unfortunately, the suggested non-Boltzmann distribution cannot be directly confirmed experimentally, as the $CH(A$-$X)$ spectra obtained in this study, even under maximum spectral resolution, possess a rather complex structure due to the partial overlap of the Q, R, and P branches for rotational numbers $J > 9$.

It is known that for Ar plasma in a humid environment, $T_{rot} = T_{gas}$ in the case of the OH band only if the lowest rotational levels are considered.[24] The presence of the TEOS precursor in the gas phase, however, may strongly influence T_{rot} values and TEOS dissociation itself has to be taken into account. To investigate this effect, T_{rot} obtained (using OH band) with and without precursor has been analyzed. The temperature calculated from the OH spectrum in Ar is 382 ± 50 K which is in reasonable agreement with the results obtained for Ar/ TEOS mixtures (see Table 2).

It is possible to assume T_{rot} (OH) $\approx T_{gas}$ also in the presence of a small amount of precursor, as its dissociation does not affect generation and excitation of OH radicals due to a very low concentration. Obviously, due to a strong discrepancy between T_{rot} obtained with different emitting species, an independent measurement of the gas temperature by the Rayleigh scattering technique is required for cross-validation. Rayleigh scattering, in spite of its high accuracy, has its own limitations, for example, interference with the Mie scattering signal in dust-containing plasmas.[46] The mentioned effect can be seen in Figure 7b, as measured during the actual deposition process. As a consequence, in the case of the Ar/TEOS mixture, it is impossible to measure T_{gas} by Rayleigh scattering due to the Mie scattering signal appearing during the nucleation process in the gas phase. Correspondingly, laser scattering was only used in pure Ar plasma.

By taking into account the respective experimental errors, the results show that T_{gas} measured by Rayleigh scattering at the time positions corresponding to the positive and negative voltage peak (see Table 3) is close to the values estimated by the OH(A-X) band.

In conclusion, the rotational distribution of OH(A) in Ar/TEOS plasmas could be used for T_{gas} measurement, taking into account the limitation relevant to filamentary Ar plasmas, while a strong overestimation of T_{gas} has been revealed in the case of N_2 and CH emission. As a result, in the latter cases, the rotational temperature is
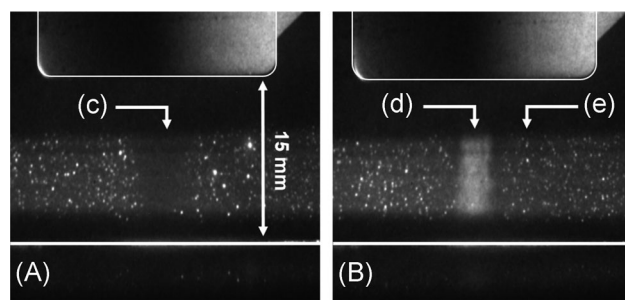
FIGURE 7 Rayleigh scattering images in (A) pure Ar or (B) Ar/TEOS (tetraethyl orthosilicate) mixture without synchronization. Scattering was induced by laser light at 532 nm: (c) Rayleigh scattering region, (d) Mie scattering of nanoparticles nucleated during the gas-phase process, (e) Mie scattering on dust in ambient air

TABLE 3 Comparison of gas temperature results obtained by OES (T_{rot}) and Rayleigh scattering at different time delays (see Figure 3)

Time delay (µs)	T_{rot} (OH band) (K)	Rayleigh scattering (K)
5	410 ± 50	390 ± 15
25	320 ± 50	310 ± 15
45	390 ± 50	340 ± 15

Abbreviation: OES, optical emission spectroscopy.

the only representative of the different production processes and cannot be used to obtain a good estimation of T_{gas}.

3.2 | Electron density

TEOS fragmentation and reactive species production are known to be controlled by electron impact reactions and argon metastables collisions during the positive and negative current peaks of a pulsed Ar discharge.[47,48] To correlate the APPJ discharge behavior with electron kinetics and shed light on the complexity of the gas-phase mechanisms in Ar/TEOS plasmas, a time-resolved measurement of electron density has also been undertaken in our work, using the Stark broadening approach. Indeed, Stark broadening of H_α and H_β lines remains one of the most suitable methods for electron density determination in the case of relatively dense plasmas ($n_e > 10^{20}$ m^{-3}).[27]

Even though the most reliable way to estimate electron density implies the H_β emission line (486.14 nm), the usability of the H_α line (656.28 nm) has also been demonstrated by several authors.[26,27] Figure 8 shows an example of time-resolved H_α line evolution used for electron density calculations in the case of Ar/TEOS plasma, starting from $t = -8$ µs (i.e., before the beginning of the positive voltage pulse) to $t = 49$ µs (end of the negative voltage pulse). As illustrated in Figure 3, at $t = -6$ µs, the discharge current rise begins and consequently (see Figure 8) the H_α intensity reaches the maximum. Afterward, its intensity decreases by approximately 50% during the subsequent 3 µs, most likely due to electron–ion recombination,[49,50] and further decreases by about 90% until the end of the positive voltage pulse. The H_α emission after the falling edge of the positive voltage pulse appears too weak for reliable Stark broadening calculation and was excluded from analysis. In contrast, the H_α intensity at $t = 37$ µs (negative peak) is stronger compared with the positive peak case, decreasing more than 50% during the subsequent 3 µs. The H_α intensity increases again after

the voltage falling edge (see Figure 9c) pointing out a rather strong secondary discharge taking place during the negative half period. As a consequence, the negative half period ($n_{e,max} \sim 10^{23}$ m^{-3}) is characterized by higher n_e values compared with the positive one ($n_{e,max} \sim 10^{22}$ m^{-3}), which is also reflected in the temporal dynamics of n_e. The Stark broadening method introduces an error of about 10% in n_e estimation for relatively high-density values ($n_e > 10^{20}$ m^{-3}), while an error of at least 20% is found in the case of low electron density ($n_e < 10^{20}$ m^{-3}).[29]

3.3 | Phase-resolved measurements

From Figure 9, it is clear that the n_e dynamics described above (Figure 9c) clearly correlates with excited species production in Ar/TEOS plasmas (Figure 9e–i). The time-resolved emission profiles of the excited species, such as O atoms, N_2 molecules, and OH and CH radicals, could provide additional information to understand which excitation processes are dominant during the plasma evolution.

Few phase-resolved emission intensity patterns can be observed in Figure 9, namely the "multi-peak" behavior of 3p →3s O I and CH $A\ ^2\Delta \to X\ ^2\Pi$ (0,0) transitions at 777.4 and 431.3 nm is presented in Figure 9f, i) while the "double-peak" behavior of N_2 C $^3\Pi_u \to B^3\Pi_g$ (0,0) and OH $A^2\Sigma^+ \to X^2\Pi_i$ (0,0) transitions (appearing at 337.1 and 308.9 nm, respectively) is shown in Figure 9g,h. In the first case, the relative intensities at $t = -6$ µs (positive half period) and at $t = 37$ µs (negative half period) are comparable despite the previously described discrepancy detected in terms of n_e. In contrast, the "double-peak" behavior resembles the n_e profile in terms of the relative intensities ratio between the peaks. A short discussion suggesting possible reasons for such behaviors is given below.
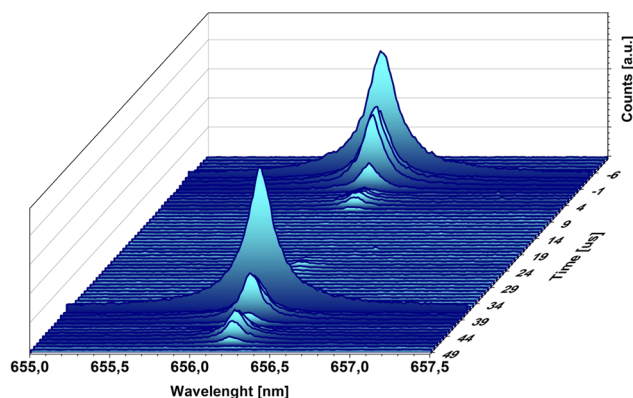
FIGURE 8 Time-resolved H_α emission peak at 655.28 nm with a time-step of 1 µs and 0.048 nm of spectral resolution
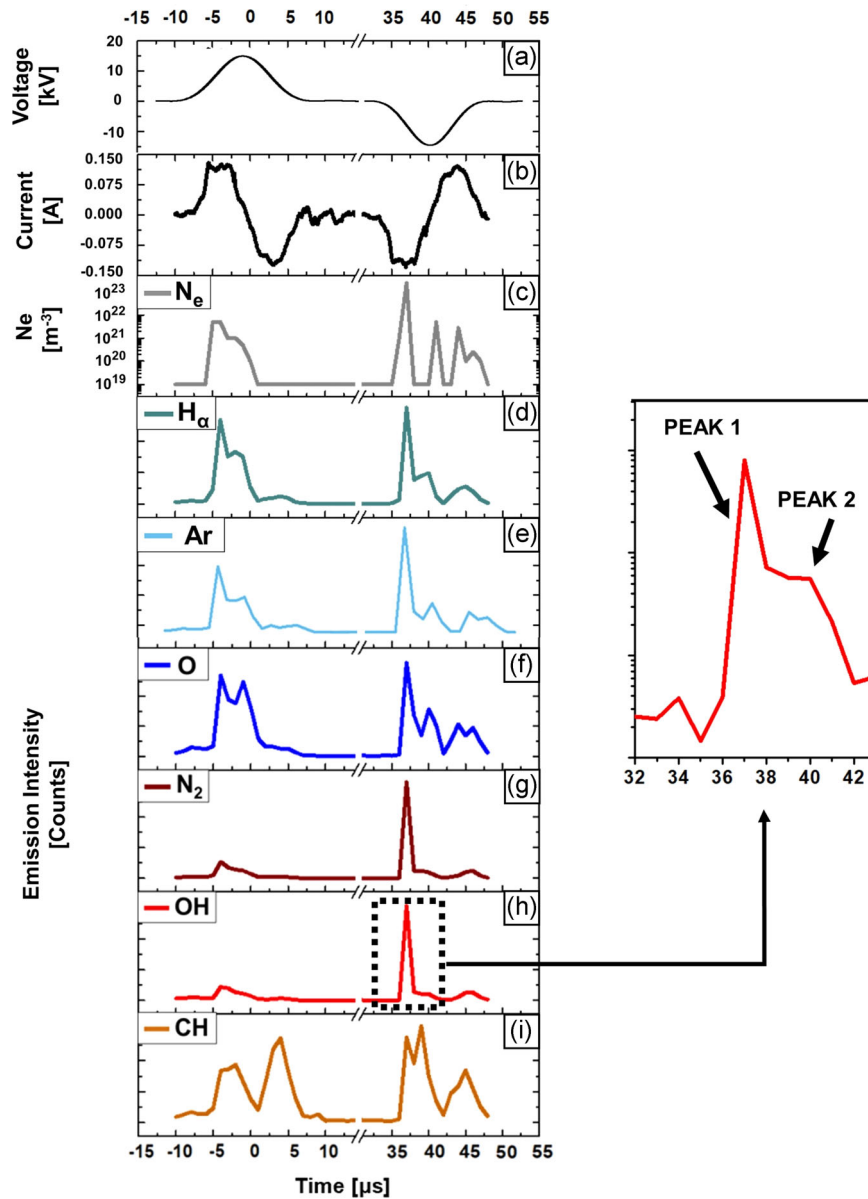
FIGURE 9 Time-resolved reactive species emission: (a) applied voltage, (b) current, (c) electron density, (d) H_α emission lines at 655.28 nm, (e) Ar emission lines at 696.6 nm, (f) O atom emission lines at 777.41 nm, (g) N_2 emission lines at 337.1 nm, (h) OH emission lines at 308.9 nm, (i) CH emission lines at 431.3 nm

It is well known that the presence of the O(3p) excited state (the upper state for the observed O emission in Figure 9) in the atmospheric pressure Ar discharges can be ascribed to O_2 molecular dissociation by electron impact ($O_2 + e \rightarrow O + O^* + e$), Penning ionization of O_2 involving Ar metastables ($Ar^m + O_2 \rightarrow Ar + O_2^+ + e$), direct excitation process of ground state O ($O + e \rightarrow O^* + e$), or dissociative excitation of the water molecules (see Equations (3) and (4)).[51] The O_2 electron impact dissociation or Penning processes, subsequent to ambient air diffusion into the plasma discharge, do not contribute to O(3p) excited state production, therefore, the most probable explanation of the "multi-peak" behavior is the presence of water vapor traces in the Ar flow. In this regard, as suggested by Beenakker et al.,[52]

O(3p) excited atoms are produced by the dissociative excitation of H_2O:

$$H_2O\,(X) + e \rightarrow O(3p^5P) + H_2(X^1\Sigma_g^+) + e\ (E_{threshold} = 15.7\ \text{eV}), \tag{3}$$

$$H_2O\,(X) + e \rightarrow O(3p^5P) + H + H + e\ (E_{threshold} = 20.2\ \text{eV}). \tag{4}$$
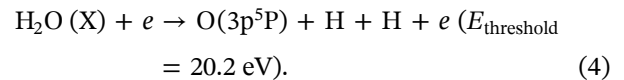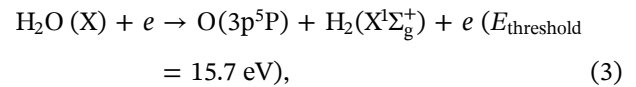
Hence, the O(3p) state production is likely limited by the dissociation rate of H_2O molecules reaching a saturation level at the time delay corresponding to both peaks due to the very low amount of water in the discharge, as confirmed by time-resolved fast imaging of the excited O atoms.

However, due to diffusion of the surrounding air molecules, the maximum N_2 emission appears at the $37\,\mu s$ time period as a double-peak, which is generated because of electron or Ar^m collisions with N_2 ground state molecules:

$$N_2(X^1\Sigma_g^+) + e \rightarrow N_2(C^3\Pi_u) + e \; (E_{\text{threshold}} = 20.2 \text{ eV}),$$
(5)

$$N_2(X^1\Sigma_g^+) + Ar^m \rightarrow N_2(C^3\Pi_u) + Ar,$$
(6)
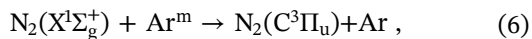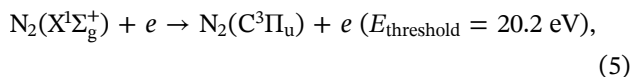
and further electron impact reactions between the pre-excited N_2 ($B^3\Pi_g$) and N_2 ($A^3\Sigma_u^+$) states.[53]

A "double-peak" behavior has also been identified for OH(A-X) emission. In Ar plasmas the excited OH(A) radicals can be produced either by dissociative electron excitation of water molecules

$$H_2O^* + e \rightarrow OH(A^2\Sigma^+) + H + e \; (E_{\text{threshold}} = 9.1 \text{ eV}),$$
(7)
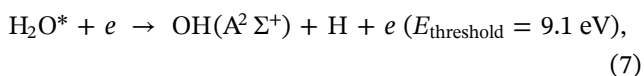
or by Ar^m–H_2O reactions[54]:

$$H_2O^* + Ar^m \rightarrow OH(A^2\Sigma^+) + H + Ar.$$
(8)

If the mechanism (7) is dominant, OH(A) radicals would present a "multi-peak" behavior reaching a saturation level; while, the second pathway should result in a "double-peak" emission profile, which takes place in our case. This dominant process confirmed in Figure 9h, does not preclude the presence of the other mechanisms, such as direct electron impact excitation of dissociated OH(X) radicals, which contributes widely to the population of excited OH at rotational levels with $J < 12$.

$$OH(X^2\Pi) + e \rightarrow OH(A^2\Sigma^+) + e \; (E_{\text{threshold}} = 4 \text{ eV}).$$
(9)
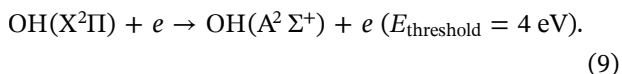
To discuss CH temporal behavior (Figure 9i), it is necessary to take into account the main TEOS dissociation products generated during the deposition process. As mentioned above, the TEOS molecules after their collisions with electrons and Ar^m may produce stable fragments, such as CH_3–CH, which can be further dissociated forming ground state CH(X) or excited CH(A) radicals. In our case, the found CH(A) emission possesses a "multi-peak" behavior, as the CH(A) state population is probably limited by the dissociation rate of CH_3–CH fragments considering the low amount of precursor injected to the APPJ. Single-step dissociative excitation processes of CH_3–CH fragments or collision

with Ar^m are unknown, however, considering that the typical electron energy is close to 1 eV in the case of Ar APPJ, it is probable that most of the CH(A) emission occurs due to the electron impact:

$$CH(X^2\Delta) + e \rightarrow CH(A^2\Pi) + e \; (E_{\text{threshold}} = 3\text{–}4 \text{ eV}).$$
(10)
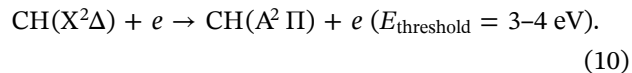
In addition, unlike the other radicals, the CH(A) emission intensity also forms secondary peaks, corresponding to the second current pulses, which confirm that CH(A) time-resolved behavior is caused mainly by low threshold energy reactions or collisions with other excited radicals such as OH.

In addition, as shown in Figure 9i, the phase-resolved emission intensity pattern of CH is also slightly delayed in time with respect to the other excited species. This delay of about $1\text{–}2\,\mu s$ could be related to the occurrence of simultaneous CH ground state excitation processes induced by electron or Ar^m collisions and consequent multistep depopulation processes. Indeed, different CH states, such as CH(B) or CH(C), or CH(A) with higher vibrational numbers can populate the CH (A, $\nu = 0$) state before reaching the ground state, thus retarding the 431.3 nm transition time-evolution. However, further experimental tests are required to confirm the suggested mechanism.

3.4 | Time-resolved discharge imaging

Spatial distribution of the excited species in the active plasma region may further clarify the most important nucleation and thin film growth processes occurring both in the gas phase and at the gas–substrate interface. To understand the main formation mechanisms involved in the atmospheric pressure deposition process, a detailed study of the evolution of streamers formed between the jet electrodes is required, which is described in this section. The phase-resolved 2D spatial emission of Ar, atomic O, N_2, OH, and CH excited species is presented in Figure 10 during the positive/negative pulses and between the current peaks in the case of the Ar/TEOS mixture. As can be seen from the voltage waveform, all images were obtained after the voltage falling edge, corresponding to the second current peak.

As shown in Figure 1, the APPJ configuration used in this study is composed of an HV single electrode corona jet facing grounded plate covered with a dielectric barrier. Accordingly, the discharge is characterized by an intensive plasma region located close to the tip of the HV electrode, as confirmed by the Ar I emission at the top of Figure 10. In addition, a strong Ar line emission,
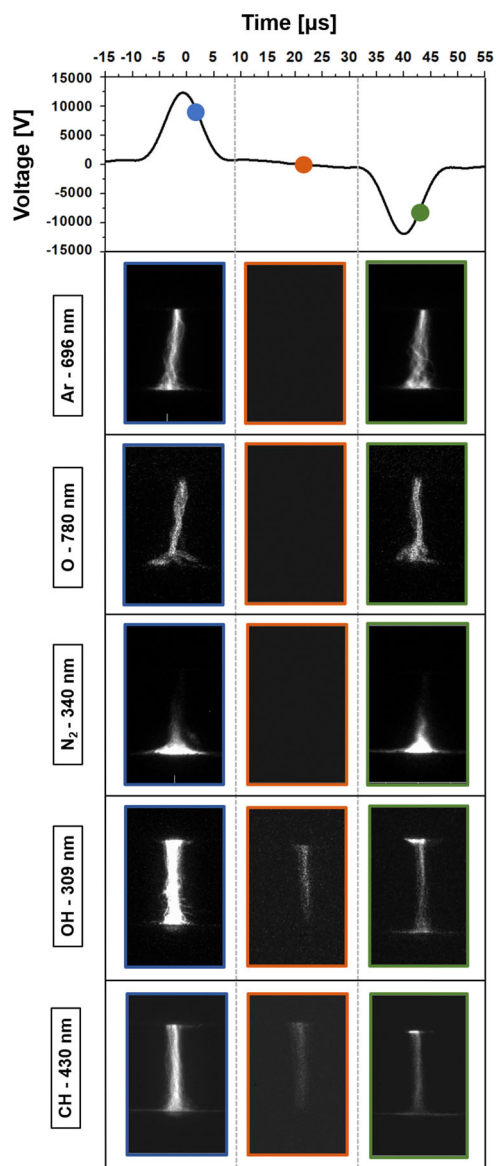
FIGURE 10 Time-resolved fast imaging of the excited: Ar atoms (20 accumulations), O atoms (single shot), N_2 molecules (20 accumulations), OH, and CH radicals (20 accumulations)

induced by the charges deposited on the surface of the dielectric plate during the primary discharge, also occurs next to the ground electrode, in analogy with classical dielectric barrier discharge configuration. The image acquired between the peaks confirms the presence of Ar excited species only during the active discharge phase characterized by high electron density, as shown in Figure 9.

As mentioned previously, in the case of open-air argon plasma discharges, the influence of the ambient air diffusion on the excited species distribution has to be taken into account. From the phase-resolved 2D images of the excited N_2, it is possible to deduce that the air back diffusion and admixing is maximum near the ground electrode, probably due to the turbulence induced by Ar

gas flow pointed toward the dielectric surface.[55] As shown in Section 3.3, N_2 emission is strictly related to the diffusion of the surrounding air, while the O atom emission seems to be mostly dependent on the dissociative excitation of the water molecules present in Ar flow. The 2D images of excited O atom and N_2 (Figure 10) confirm these different particle sources, as the O atom emission appears constant over the entire discharge, whereas N_2^* emission is localized near the bottom plate.

The effect of TEOS admixing on the discharge structure has been also studied by 2D imaging of the OH(A) emission band (as shown in Figure 11). The data were acquired in this case during the negative voltage peak with and without precursor. We observed that TEOS injection reduces OH emission intensity all over the plasma discharge except the region downstream of the HV tip. This effect is correlated with the fact that the addition of complex chemical compounds, like TEOS, results in electron temperature reduction in the discharge due to a change in the energy transfer efficiency between electrons and heavy species.

By comparing the data shown in Figures 10 and 11, it is clear that OH(A) and CH(A) radicals show almost identical distributions in terms of the streamer shape, emission spatial distribution, and relative intensities. This similarity in the presence of high-emission zones near the HV tip confirms that in both cases both OH(A) and CH(A) radical generation happens via strong influence of Ar metastables. Moreover, the CH(A) and OH(A) emission is detectable between the current peaks, confirming the key role of Ar metastable production of both radicals.[56]

3.5 | Thin-film surface characterization

Si-based thin films have been deposited onto PP foils with 60 s of treatment time. ATR-FTIR and SEM analysis have been performed to point out the most significant thin film features and their relationship with the gas-phase deposition process previously identified.
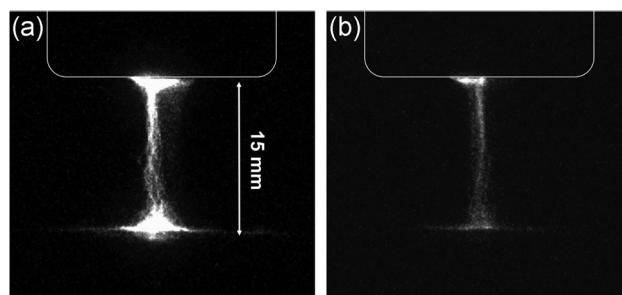
FIGURE 11 Single-shot OH images gained at 42 μs of delay time (negative peak) in (a) Ar or (b) Ar/TEOS (tetraethyl orthosilicate) mixture

FIGURE 12 Attenuated total reflectance-Fourier-transform infrared spectrum of the SiO$_2$-like thin films deposited in the Ar/TEOS (tetraethyl orthosilicate) mixture for 60 s of treatment time
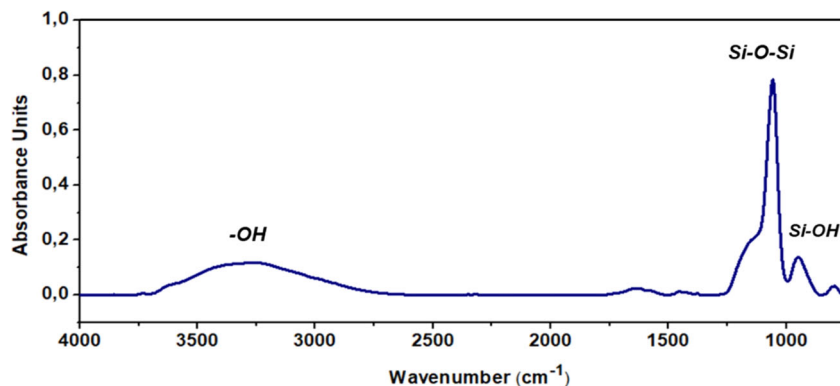
As is known, the high number of energetic electrons and argon metastable atoms produced during the process take part in the dissociation of TEOS molecules leading to hydrocarbons and Si-containing fragments. Despite this organic–inorganic behavior of TEOS molecules, many researchers have already reported the use of atmospheric pressure plasmas for the synthesis of high-quality SiO$_2$-like coatings possessing excellent properties in terms of dielectric strength, optical transparency, and barrier performance.[1,57] The chemical composition of the thin films obtained in the Ar/TEOS mixture by preserving operational conditions used for the gas-phase characterization is shown in Figure 12.

As disclosed by Starostin et al.,[1] in the case of Ar/N$_2$/O$_2$/TEOS plasma, different absorption bands can be used to evaluate the inorganic behavior of the plasma-polymerized thin film. In detail, the dominant absorption peaks in the region between 1,040 and 1,250 cm^{-1} correspond to the Si–O–Si unit stretching vibrations, while the peak around 930 cm^{-1} and the broad band at 2,800–3,700 cm^{-1} are associated with silanol groups (Si–OH) and hydroxyl groups (–OH), respectively. In our case, the predominant synthesis of inorganic structures is also confirmed by the absence of absorption peaks related to C–H and C–O stretching vibrations.

Moreover, top-view SEM images presented in Figure 13, reveal a thin film microstructure with a large amount of powder-like incorporations as well as the presence of defects on the surface of the deposits.

The deposition of thin films with high roughness is often caused by the predominant role of gas-phase nucleation processes and subsequent deposition of dust particles on the target.[58] However, in our case, the dust particles seem densely packed on the PP foil, and consequently, the possibility that the other formation mechanisms will occur at the gas–substrate interface cannot be excluded. One of the particular features of the deposited coatings is the presence of large cracks over the whole substrate surface, as seen in Figure 13. The crack formation on thin films was discussed in detail by Petersen et al.[38] for the case of the Si-based coating deposited onto thermosensitive substrates. It was revealed that the mechanism is related to the induced thermal stress and the consequent stretching of the polymeric substrate during deposition. These morphological results seem in line with the gas temperature values presented in Section 3.1 and possible gas-phase nucleation processes detected by the Rayleigh scattering technique in the mixture Ar/TEOS.
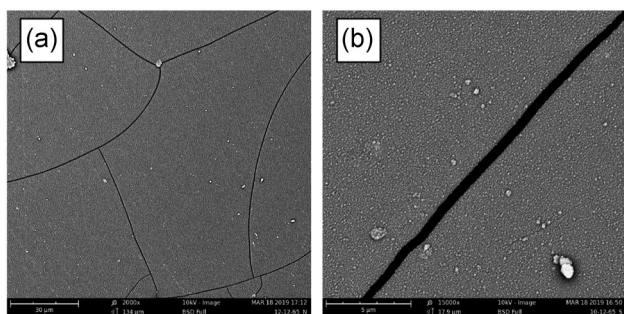
FIGURE 13 Scanning electron microscopic pictures of the thin films deposited on polypropylene substrate for 60 s of treatment time acquired by using: (a) ×2,000 magnification, (b) ×15,000 magnification

4 | CONCLUSIONS

The effect of TEOS addition on the physical and chemical properties of an APPJ source operating in Ar is studied in detail by OES, 2D optical imaging, and Rayleigh scattering techniques. It was confirmed that the rotational temperature of the N$_2$(C-B) transition, equal to 550 K, cannot be used for reliable estimation of the gas temperature also in the case of Ar/TEOS plasmas, due to quasi-resonance processes with Ar metastables. However, the rotational temperature of OH excited radicals, obtained in the assumption of non-Boltzmann rotational distribution, is significantly lower than the one obtained

with N_2 molecular bands, and its mean value (409 K) is in a good agreement with the Rayleigh scattering results.

For the first time, the possibility of using the CH(A-X) transition for gas temperature measurement in an atmospheric pressure Ar/TEOS plasma is confirmed. In this case, the Ar metastables as well as the electron impact reactions with TEOS fragments are presumably playing a key role in the CH(A) radical formation in nonthermal equilibrium leading to an overestimation of the gas temperature (590 K) by CH emission bands in the investigated type of discharges.

The phase-resolved measurements as well as the 2D imaging data of the excited species, along with the time-resolved electron density behavior were used to reveal the predominant production mechanisms of the O(3p), $N_2(C)$, OH(A), CH(A) excited states in the discharge. It was concluded that the O atom emission is determined mostly by the dissociative excitation of water molecules contained in Ar gas flow, whereas $N_2(C)$ is the product of Ar^m and electron reactions with N_2 ground state molecules appearing due to the surrounding air diffusion to the active plasma zone. As expected, in the case of atmospheric pressure deposition, Ar metastables also play a dominant role in OH and CH excited radical generation. Finally, from the spatial distribution of CH(A), Rayleigh scattering images and SEM results, it has been concluded that the most important nucleation process takes place in the gas phase.

ACKNOWLEDGMENTS

ORCID

Federica Barletta http://orcid.org/0000-0001-8920-9203

REFERENCES

[1] S. A. Starostin, M. Creatore, J. B. Bouwstra, M. C. M. van de Sanden, H. W. de Vries, *Plasma Process. Polym.* **2015**, *12*, 503.

[2] R. Förch, A. N. Chifen, A. Bousquet, H. L. Khor, M. Jungblut, L. Q. Chu, Z. Zhang, I. Osey-Mensah, E. K. Sinner, W. Knoll, *Chem. Vap. Dep.* **2007**, *13*, 280.

[3] T. Yokoyama, M. Kogoma, S. Kanazawa, T. Moriwaki, S. Okazaki, *J. Phys. D: Appl. Phys.* **1990**, *23*, 374.

[4] S. E. Babayan, J. Y. Jeong, V. J. Tu, J. Park, G. S. Selwyn, R. F. Hicks, *Plasma Sources Sci. Technol.* **1998**, *7*, 286.

[5] R. Morent, N. De Geyter, S. Van Vlierberghe, P. Dubruel, C. Leys, L. Gengembre, E. Schacht, E. Payen, *Prog. Org. Coat.* **2009**, *64*, 304.

[6] F. Massines, N. Gherardi, A. Fornelli, S. Martin, *Surf. Coat. Technol.* **2005**, *200*, 1855.

[7] J. Schäfer, R. Foest, A. Quade, A. Ohl, J. Meichsner, K. D. Weltmann, *Eur. Phys. J.* **2009**, *54*, 211.

[8] J. Pulpytel, V. Kumar, P. Peng, V. Micheli, N. Laidani, F. Arefi-Khonsari, *Plasma Process. Polym.* **2011**, *8*, 664.

[9] X. Lu, G. V. Naidis, M. Laroussi, S. Reuter, D. B. Graves, K. Ostrikov, *Phys. Rep.* **2016**, *630*, 1.

[10] A. Schutze, J. Y. Jeong, S. E. Babayan, J. Park, G. S. Selwyn, R. F. Hicks, *IEEE Trans. Plasma Sci.* **1998**, *26*, 1685.

[11] X. Lu, M. Laroussi, V. Puech, *Plasma Sources Sci. Technol.* **2012**, *21*, 034005.

[12] R. Reuter, D. Ellerweg, A. von Keudell, J. Benedikt, *Appl. Phys. Lett.* **2011**, *98*, 111502.

[13] C. Huang, C. H. Liu, S. Y. Wu, *Surf. Interface Anal.* **2009**, *41*, 44.

[14] L. Körner, A. Sonnenfeld, R. Heuberger, J. H. Waller, Y. Leterrier, J. A. E. Månson, P. R. von Rohr, *J. Phys. D: Appl. Phys.* **2010**, *43*, 115301.

[15] P. A. Premkumar, S. A. Starostin, M. Creatore, H. de Vries, R. M. J. Paffen, P. M. Koenraad, M. C. M. van de Sanden, *Plasma Process. Polym.* **2010**, *7*, 635.

[16] C. O. Laux, T. G. Spence, C. H. Kruger, R. N. Zare, *Plasma Sources Sci. Technol.* **2003**, *12*, 125.

[17] G. Dilecce, *Plasma Sources Sci. Technol.* **2014**, *23*, 015011.

[18] M. Goujon, T. Belmonte, G. Henrion, *Surf. Coat. Technol.* **2004**, *188–189*, 756.

[19] A. Granier, C. Vallée, A. Goullet, K. Aumaille, G. Turban, *J. Vac. Sci. Technol. A* **1999**, *17*, 2470.

[20] F. Barletta, A. Liguori, C. Leys, V. Colombo, M. Gherardi, A. Nikiforov, *Mater. Lett.* **2018**, *214*, 76.

[21] A. Liguori, A. Pollicino, A. Stancampiano, F. Tarterini, M. L. Focarete, V. Colombo, M. Gherardi, *Plasma Process. Polym.* **2016**, *13*, 375.

[22] D. R. Stull, *Ind. Eng. Chem.* **1947**, *39*, 517.

[23] P. Bruggeman, D. C. Schram, M. G. Kong, C. Leys, *Plasma Process. Polym.* **2009**, *6*, 751.

[24] P. Bruggeman, N. Sadeghi, D. C. Schram, V. Linss, *Plasma Sources Sci. Technol.* **2014**, *23*, 023001.

[25] A. Sarani, A. Y. Nikiforov, C. Leys, *Phys. Plasmas* **2010**, *17*, 063504.

[26] P. Bruggeman, D. Schram, M. Á. González, R. Rego, M. G. Kong, C. Leys, *Plasma Sources Sci. Technol.* **2009**, *18*, 025017.

[27] A. Y. Nikiforov, C. Leys, M. Á. González, J. L. Walsh, *Plasma Sources Sci. Technol.* **2015**, *24*, 034001.

[28] Q. Xiong, A. Nikiforov, N. Britun, R. Snyders, C. Leys, X. Lu, *J. Appl. Phys.* **2011**, *110*, 073302.

[29] H. Griem, *Spectral Line Broadening by Plasmas*, Academic Press, New York, NY **1974**.

[30] S. Hofmann, A. F. H. van Gessel, T. Verreycken, P. Bruggeman, *Plasma Sources Sci. Technol.* **2011**, *20*, 065010.

[31] M. A. Gigosos, M. Á. González, V. Cardeñoso, *Spectrochim. Acta, Part B* **2003**, *58*, 1489.

[32] R. B. Miles, W. R. Lempert, J. N. Forkey, *Meas. Sci. Technol.* **2001**, *12*, R33.

[33] M. Sneep, W. Ubachs, *J Quant. Spectrosc. Radiat. Transfer* **2005**, *92*, 293.

[34] P. Bruggeman, R. Brandenburg, *J. Phys. D: Appl. Phys.* **2013**, *46*, 464001.

[35] A. F. H. van Gessel, E. A. D. Carbone, P. J. Bruggeman, J. J. A. M. van der Mullen, *Plasma Sources Sci. Technol.* **2012**, *21*, 015003.

[36] P. J. Cullen, V. Milosavljevic, *Prog. Theor. Exp. Phys.* **2015**, 063J01.

[37] M. Abbasi-Firouzjah, S. I. Hosseini, M. Shariat, B. Shokri, *J. Non-Cryst. Solids* **2013**, *368*, 86.

[38] J. Petersen, J. Bardon, A. Dinia, D. Ruch, N. Gherardi, *ACS Appl. Mater. Interfaces* **2012**, *4*, 5872.

[39] K. Okimura, N. Maeda, *J. Vac. Sci. Technol.* **1998**, *16*, 3157.

[40] S. Kawaguchi, H. Higuchi, H. Li, K. Denpoh, K. Takahashi, K. Satoh, *Jpn. J. Appl. Phys.* **2019**, *58*, 066003.

[41] L. Le Brizoual, A. Granier, P. Briaud, in *Proc. XXIII Int. Conf. Phenomena in Ionized Gases*, Toulouse, France, Université Paul Sabatier, 1997, III.

[42] L. G. Piper, J. E. Velazco, D. W. Setser, *J. Chem. Phys.* **1973**, *59*, 3323.

[43] M. Steinbauer, J. Giegerich, K. H. Fischer, I. Fischer, *J. Chem. Phys.* **2012**, *137*, 014303.

[44] J. Luque, M. Kraus, A. Wokaun, K. Haffner, U. Kogelschatz, B. Eliasson, *J. Appl. Phys.* **2003**, *93*, 4432.

[45] G. Dinescu, A. de Graaf, E. Aldea, M. C. M. Sanden, *Plasma Sources Sci. Technol.* **2001**, *10*, 513.

[46] L. Mangolini, *J. Phys. D: Appl. Phys.* **2017**, *50*, 373003.

[47] C. P. Klages, A. K. Czerny, J. Philipp, M. M. Becker, D. Loffhagen, *Plasma Process. Polym.* **2017**, *14*, e1700081.

[48] M. Ducrepin, J. Dike, R. B. Siegel, V. Tarnovsky, K. Becker, *J. Appl. Phys.* **1993**, *73*, 7203.

[49] N. Y. Babaeva, G. V. Naidis, *J. Electrost.* **2001**, *53*, 123.

[50] S. Hübner, S. Hofmann, E. M. van Veldhuizen, P. J. Bruggeman, *Plasma Sources Sci. Technol.* **2013**, *22*, 065011.

[51] G. Y. Park, Y. J. Hong, H. W. Lee, J. Y. Sim, J. K. Lee, *Plasma Process. Polym.* **2010**, *7*, 281.

[52] C. I. M. Beenakker, F. J. De Heer, H. B. Krop, G. R. Möhlmann, *Chem. Phys.* **1974**, *6*, 445.

[53] Q. Xiong, X. Lu, J. Liu, Y. Xian, Z. Xiong, F. Zou, C. Zou, W. Gong, J. Hu, K. Chen, X. Pei, Z. Jiang, Y. Pan, *J. Appl. Phys.* **2009**, *106*, 083302.

[54] T. Shirafuji, Y. Ogura, Y. Himeno, *Jpn. J. Appl. Phys.* **2014**, *53*, 010211.

[55] E. Traldi, M. Boselli, E. Simoncelli, A. Stancampiano, M. Gherardi, V. Colombo, G. S. Settles, *EPJ Tech. Instrum.* **2018**, *5*, 4.

[56] D. Merche, N. Vandencasteele, F. Reniers, *Thin Solid Films* **2012**, *520*, 4219.

[57] F. Crisostomo, R. A. Taylor, T. Zhang, I. Perez-Wurfl, G. Rosengarten, V. Everett, E. R. Hawkes, *Renewable Energy* **2014**, *72*, 79.

[58] T. Fujimoto, K. Okuyama, M. Shimada, Y. Fujishige, M. Adachi, I. Matsui, *J. Appl. Phys.* **2000**, *88*, 3047.

Industrial Applications of Plasmas. Her current research interests include plasma diagnostics of atmospheric pressure plasmas for thin-film deposition, plasma–surface interactions in the context of surface treatment of polymers and thin-film surface characterization techniques.

Nikolay Britun is graduated from Kiev National University (Ukraine) in 2002 and received his PhD in plasma diagnostics from the Sungkyunkwan University (South Korea), in 2008. Since 2009 he is a researcher at the Lab. Chimie des Interactions Plasma-Surface at the University of Mons (Belgium). His main interests are related to optical characterization of the low-temperature and fusion plasmas, optical emission, and absorption spectroscopy, laser-based methods for plasma diagnostics, and so forth. The main research topics currently include gas conversion by nonequilibrium discharges, characterization of magnetron sputtering discharges, laser-based diagnostics in the atmospheric plasma sources, as well as plasma interferometry.

Dr. Anton Nikiforov obtained Ph.D. in the year 2004 in the field of plasma chemistry. He has more than 15 years of experience in spectroscopy, plasma technology, and surface engineering. His research activity is essentially an experimental work that focuses on the nonequilibrium plasma-initiated chemistry, plasma processes, nanomaterials synthesis, and advanced methods of plasma spectroscopy. Ongoing studies bear on plasma–surface interactions, on new methods of chemical synthesis in the liquid phase and on the engineering of surfaces in nonequilibrium conditions.

AUTHOR BIOGRAPHIES

Federica Barletta was born in Italy in 1991. She received the Master's degree in 2016 in Energy Engineering from the University of Bologna and is currently Ph.D. student at the Department of Industrial Engineering in the field of